Selective gas detection using phase change material infused photonic crystal

Shirish Tripathi [*], Ritesh Kumar Mishra

Department of Electronics and Communication Engineering, National Institute of Technology Patna, Patna, India

A R T I C L E   I N F O

A B S T R A C T

A photonic crystal-based optical gas detector is proposed, incorporating phase change material (PCM) to modulate the sensing properties. The multi-gas detection process is designed in the range of 650 nm to 2500 nm. $Ge_2Sb_2Te_5$ (GST) is employed as a phase change material with significant optical property variations. It can exist in two self-sustaining, bi-stable phases: a crystalline GST (CGST) and an amorphous GST (AGST). The dielectrics (*i.e.*, Si, SiO_2, GST, and Au) are used in various combinations, such as Au-Si, Au-Si-SiO_2, Au-GST-SiO_2, and GST-Au. Plane light waves are used to model the nanoporous structures over a broad wavelength range (650 nm to 2500 nm). The optical spectral response of the structures, including the reflectivity spectrum, power absorption spectrum, and electric field distribution, is investigated by varying the GST thickness, dimension, and geometry of the nanoholes. Liquid ammonia has the highest selectivity of any gas from 650 nm to 1000 nm, at about 29%, whereas carbon monoxide has the maximum sensitivity of 32%. The interchanging of layers increases the sensitivity of all the gases. With a sensitivity and selectivity of 78% and 40%, respectively, carbon monoxide exhibits the greatest values.

1. Introduction

Gas detection technology has turned out to be an important aspect in determining harmful gases and their safe removal from the environment. Gas sensors are used in many different domains, including environmental degradation such as ozone gas detection, carbon monoxide detection for indoor air quality applications, and methane detection in coal fields and mines [1–3]. The primary disadvantage of a metal oxide semiconductor (MOS) sensor is its inability to function at high temperatures and its poor sensing response at room temperature. Furthermore, MOS sensor surface responses are not yet closely linked to their nanostructures to produce results that are flexible and broadly applicable. As of late, research is being done extensively on various gas sensing methods. Numerous studies have been conducted on various scenarios using improved gas sensor models and the use of PCM in gas sensing due to the broad range of applications and limitations of gas sensing technologies. The optical, electrical, and physical characteristics of PCMs can be changed during the operation of the device. Variations in the properties of GST provide a route to parametric variation during operation in purposeful applications [4,5]. Significant optical changes are seen in the metal-insulator transition whenever PCM and the nanoporous metallic structure supporting surface plasmon polaritons (SPPs) are properly coupled. This transition property can be used to further efficiently detect gases and tune resonances [6]. SPPs have been used in a variety of applications, including metamaterial structures, metal-insulator-metal (MIM) waveguide resonators, and photonic crystal structures [7,8].

---

* Corresponding author.
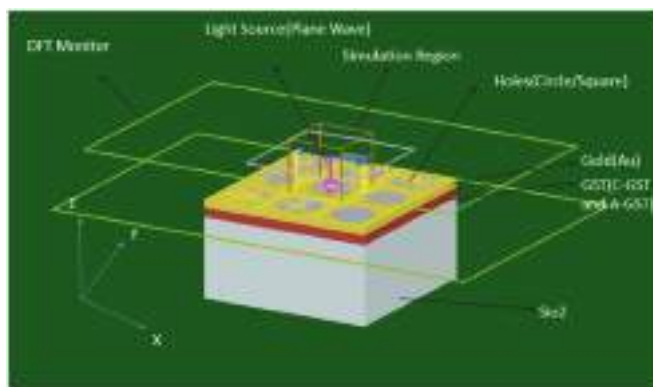 *E-mail address:* shirisht.phd20.ec@nitp.ac.in (S. Tripathi).

Fig. 1. Nanoporous photonic-crystal model and associated simulation/boundary frames with circular structure by using GST as substrate to observe the modulation or tunablity.

Surface plasmon resonance (SPR) has evolved from a cryptic physical phenomenon to an optical tool being used for biological and chemical investigations. SPR is an optical technique used to measure biomolecular interactions in real-time without the use of a label. This optical sensing approach has been employed in a wide range of applications, including biological and chemical analyte detection [9,10], environmental monitoring [11],medical diagnostics [12], drug detection [13,14], and food safety [15]. In order to make SPR sensors extremely helpful for characterizing and developing nanodevices for the aforementioned purpose, a great deal of attention is being paid to the development of nanoparticles for molecular applications. The application of SPR effects is also used in electrooptic modulators [16], tunable optical filters [17], and imaging systems [18].

In 1902, Wood noticed a thin pattern of anomalous dark and light bands in the diffracted spectrum while observing the spectrum of a continuous source of polychromatic light (white) using a diffraction grating in reflection [19]. Although he speculated about the interaction of light grating and metal, a clear answer to the phenomenon was not provided, whereas the physical phenomenon of SPR found its way to practical application in sensitive detectors. In the 1950 s, more experimentation was done on electron energy losses in gas and on thin foils. Pines and Bohm concluded that energy losses were due to the excitation of conducting electrons, creating plasmons [20]. Further research revealed the term excitation of electromagnetic 'EVANESCENT' waves, and in 1970, evanescent waves were described as a means to study ultra-thin metal films and coatings.

In 1957, surface plasmons (SPs) were first introduced theoretically by Ritchie, who introduced them to explain the characteristic losses of energy that fast electrons experience when traveling through thin metal film [21]. In 1968, Otto showed that these surface waves (plasmons) can be excited by using attenuated total reflection (ATR); thus, the prism-coupled SPR Otto configuration was studied [22]. In the same year, Kretschmann and Raether obtained the same results from different configurations of the ATR method [23]. As a result of the aforementioned, surface plasmons have drawn a lot of attention, especially when thin film studies on metal interfaces are conducted. Thus, it became a turning point in 1983 when Nylander and Liedberg, for the first time, exploited the Kretschmann configuration for gas and biomolecular detection and reported the first sensing application of SPR [24].

As narrated above, prism-based SPR has experienced some drawbacks, like bulky devices and various mechanical and optical parts being incorporated. Furthermore, it cannot be used for remote sensing [25]. In 1993, Jorgenson proposed an optical fiber-based SPR sensor where gold film was used to coat the fiber core to reveal plasmonic response [26]. Optical fiber-based SPR sensors offer numerous benefits over their conventional counterparts, including compactness, cost effectiveness, continuous fast response analysis, in situ monitoring, and a simple and flexible optical design [27]. Also, it is preferred that its core diameter be small, which is why it can be used in small areas, paving the way for remote sensing.

With the advancement in technology, microstructured optical fiber (MOF)-based plasmonic sensors have shown great development due to their high sensitivity and label-free detection [28,29]. MOF-based sensors are highly competent due to their important features like compact structure and design flexibility, controllable dispersion, and low loss. Recently, a lot of research has been done to improve the performance of SPR sensors. One of these is the photonic crystal fiber (PCF) SPR sensor, which combines SPR and PCF technology and has a flexible structure design and high sensitivity [30–33]. This works on the evanescent field principle, which ultimately results in a variation of the resonant wavelength. Miniaturization, single-mode propagation ability to control evanescent field penetration, and ease of light launching have made PCF a promising candidate for SPR sensing [34].

With the ongoing advancements in metamaterial theory and experimentation, research on tunable absorption films and metamaterial perfect absorbers (MPA) has gained significant traction in recent years [35]. Applications for polarization-independent graphene-based tunable bandwidth absorbers that may achieve high absorption rates through the coupling of localized surface plasmon resonance (LSPR) include photoelectric sensing and biomedicine [36,37]. In high-sensitivity sensors, photothermal detection, and thermal radiation, multi-band and multi-adjustable narrowband perfect absorbers based on the MPA structure are employed [38].

The active plasmatic device utilizing the phase change characteristics of GST is probably detailed in recent years since GST has peculiar properties that include high compatibility, vast permittivity change in the infrared region, high stability, and are easily reconfigurable as compared to regular semiconductors [39]. GST has found extensive applications in different nano-photonic devices such as optical memory, tunable immaculate ingesters, holographic showcase boards, etc.
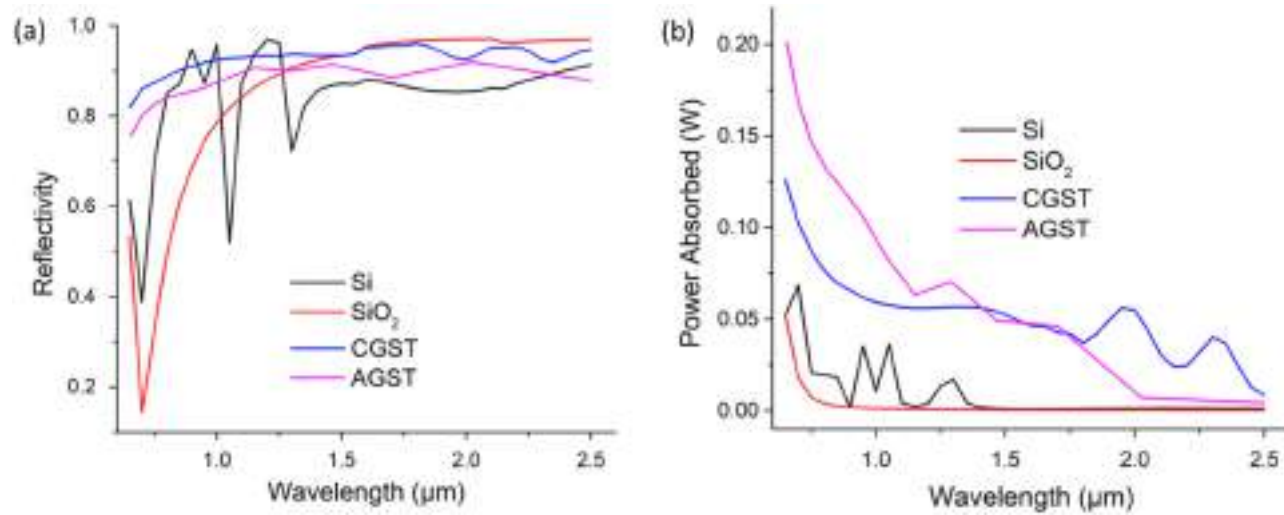
Fig. 2. Variation of (a) Reflectivity and (b) Power Absorption of Au-Si-SiO2, Au- SiO2, Au-CGST-SiO2, Au-AGST-SiO2 at 100 nm thickness when the radius of the circle is 0.150 μm.
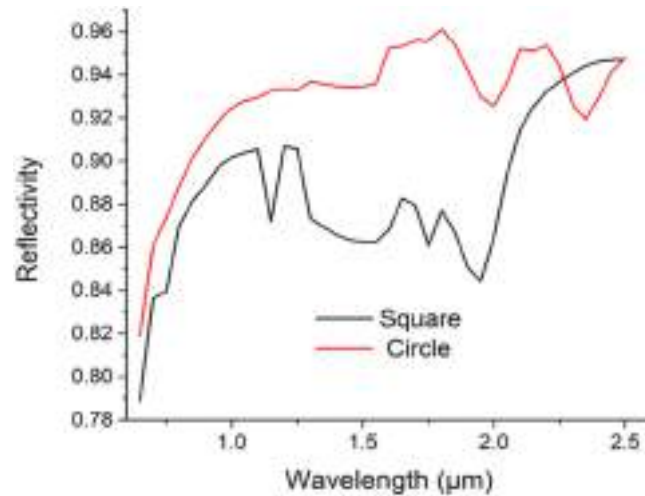
Fig. 3. Reflectivity of Au-CGST- SiO$_2$ at 100 nm thickness with different geometries.

When light is incident normally on a metal film patterned with an array of nanoholes, strong optical reflection is found at a certain optical wavelength. When combined with other materials (such as dielectrics), these nanoporous structures can be used to sense and detect a variety of gases [40]. The spectrum behavior in terms of power and position of the reflection peaks is affected by a few parameters, such as the medium's refractive index, the degree of polarization of the incident light on the sensor, the size and shape of the holes and wavelength, and the periodicity of the structures [41]. Noble metals such as gold (Au), silver (Ag), and copper (Cu) are outstanding reflectors in the infrared (IR) region and are used for producing strong absorption and reflection spectrum due to the excitation of plasmonic resonance [42]. The proposed nanoporous structure has been investigated based on finite difference time domain (FDTD) solutions using the *Lumerical* Tool.

2. Methodology

We have used four different types of nanoporous structures, namely Metal-Insulator (M-I), Metal-Semiconductor-Insulator (M-SC-I), Metal-Phase Change Material-Insulator (M-PCM-I), and Phase Change Material-Metal (PCM-M). In the first three nanoporous structures, the substrate is positioned beneath the gold layer, and holes are created in the gold layer; in the final structure, holes are created in the substrate, and the gold layer is positioned beneath it. In order to ensure minimal transmission (equivalent to zero), a 100 nm thick layer of gold is selected. This layer is significantly thicker than the penetration depth of the electromagnetic (EM) waves in the near-infrared region (NIR) and short-wavelength infrared region (SWIR). The simulations are done using the *Lumerical FDTD* tool. All the nanoporous structures are illuminated with plane waves directed along the Z-axis, and the source is kept at a distance of λ$_{max}$/2. The geometry is set based on the structure used. We have worked with circle and square geometry. The general mesh setting is set to 0.01 μm for all directions (dx=dy=dz=0.01 μm).

Due to the periodicity of the nanoporous structure, a one-unit cell of the investigated structure is simulated by using periodic boundary conditions in the X-Y plane, and perfectly matched layer (PML) is applied to the axis of propagation of the EM waves (Z-axis). A steep angle profile is used for the PML settings. Layers are set to twelve. Because of the periodic nature of the structure, symmetric boundary conditions are applied on the Y-direction, anti-symmetric constraints are applied on the X-direction, and ¼th of the unit cell is simulated to speed up the simulation and use less memory and space. We employed 2D-Z normal and 2D-Y normal index monitors to measure the index profile in the XY plane and XZ plane, respectively. We tracked reflection and transmission spectra using a 2D-Z normal DFT monitor. We employed two frequency domain power monitors (DFT monitors) to determine the reflection spectrum. One monitor is placed just above the light source to monitor the 'Total Reflection Spectrum'. The other monitor is placed on the substrate to measure the amount of light that is being transmitted through the device. The periodicity is set to nine holes per structure. The holes are of a subwavelength nature. We have examined the holes using square and circle geometries. The radius of the circle is set to 0.1 μm, 0.125 μm, and 0.150 μm. The square's width is fixed at 0.3 μm. The thickness of the GST is also varied in the range of 20 nm, from 60 nm to 120 nm. The circle with various radii has been filled with the gas to be examined. In this work, we have analyzed liquid ammonia, liquid methane, carbon dioxide, and carbon monoxide. The above gases' refractive index (n) and extinction coefficient (k) are derived from a review of the literature [43–45]. Fig. 1

3. Results and discussion

Prior to being exposed to a gas environment, variations in the optical characteristics of various substrates are simulated and compared. A sensor with a flat spectral reflectivity response is more sustainable and performs better. As seen from Fig. 2(a), by using PCMs (CGST and AGST), we can get a flat response as well as high reflectivity. Hence, the PCMs can be used for sustainable detection.
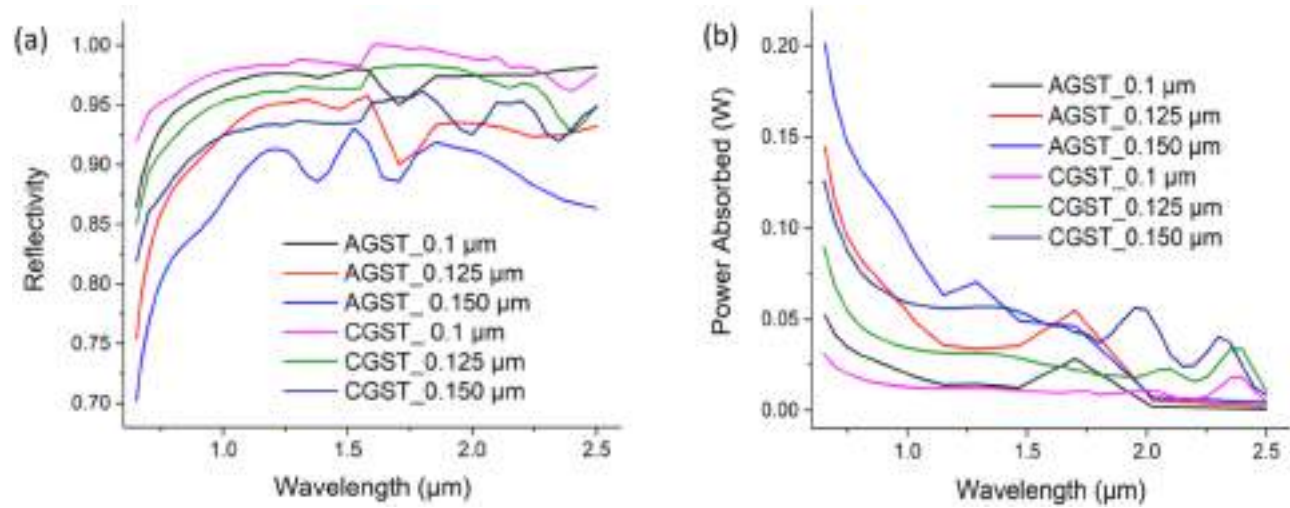
Fig. 4. Variation of (a) Reflectivity and (b) Power Absorption of Au-CGST-SiO2, Au-AGST-SiO2 at 100 nm thickness when the radius of the circle is 0.1 μm, 0.125 μm, 0.150 μm.
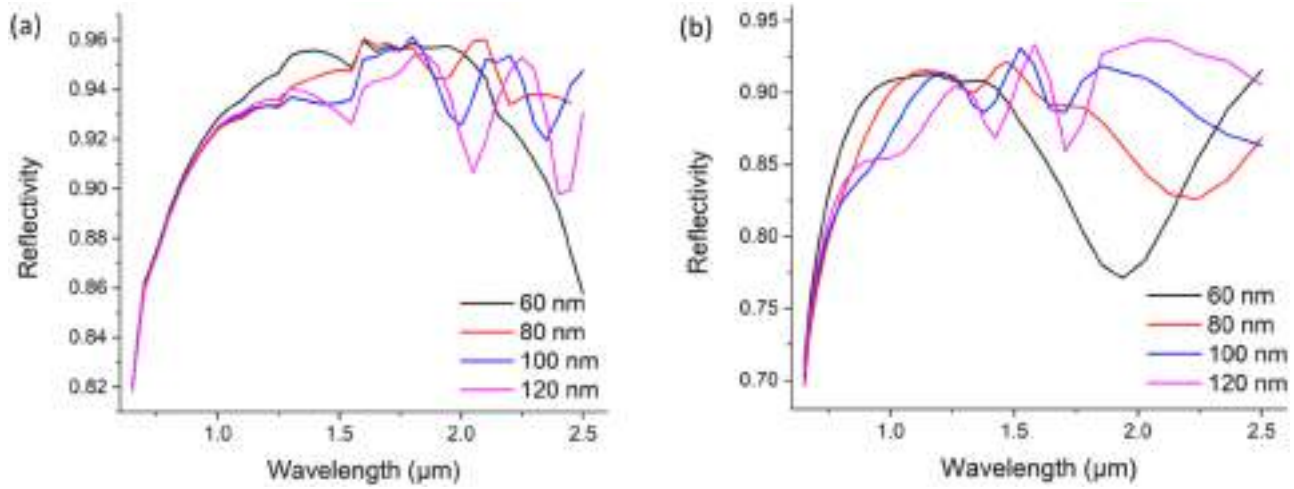
Fig. 5. Variations in reflectivity of (a) Au-CGST-SiO$_2$ (b) Au-AGST-SiO$_2$ at various thickness when the radius of the circle is 0.150 μm.
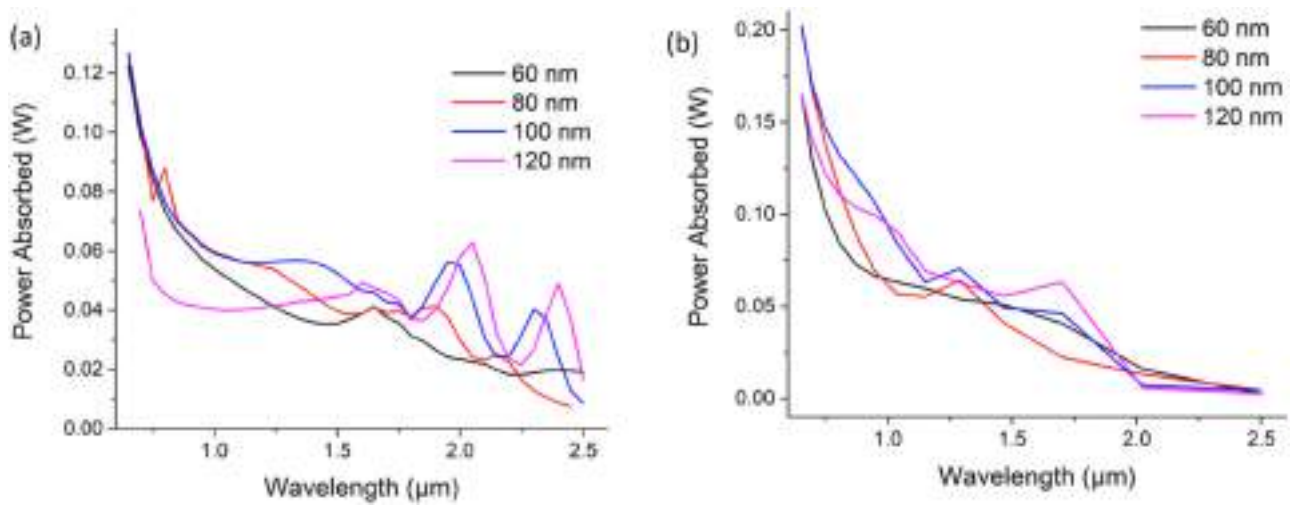
Fig. 6. Variations in power absorption of (a) Au-CGST-SiO2 (b) Au-AGST-SiO$_2$ at various thickness when the radius of the circle is 0.150 μm.
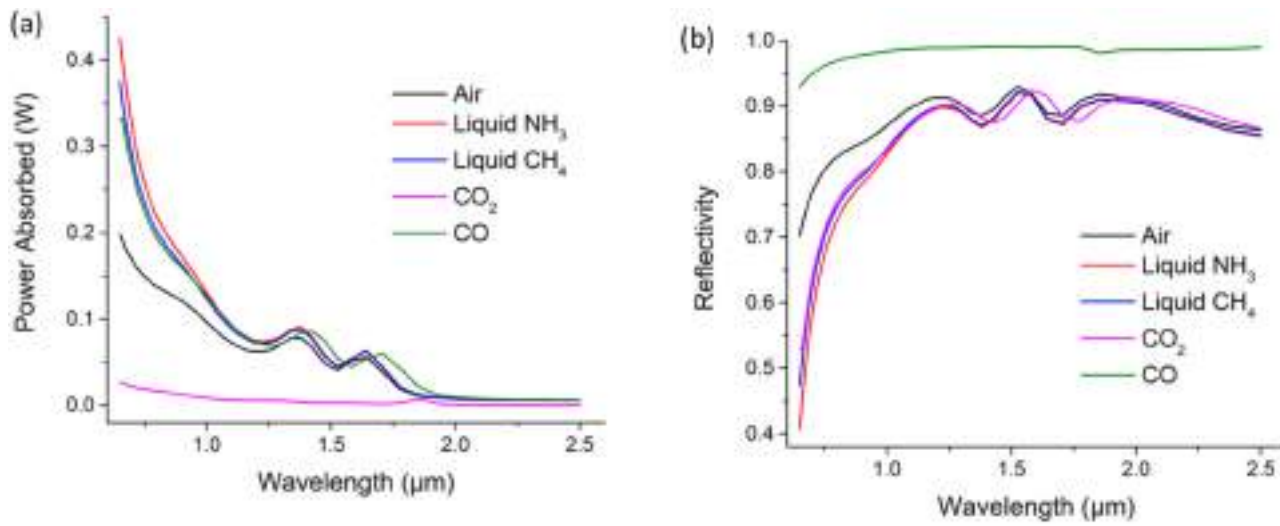
Fig. 7. Variations in (a) Power Absorption (b) Reflectivity of Au-AGST-SiO$_2$ for different gases at 100 nm thickness when the radius of the circle is 0.150 μm.

Table 1
Selectivity of gases at different wavelength *w.r.t* AGST.

Gases	Wavelength Region (650–1000 nm)	Wavelength Region (1000–2500 nm)
Liquid Ammonia	12–29 %	<4 %
Liquid methane	9–22 %	<4 %
Carbon Dioxide	8–17 %	<4 %
Carbon Monoxide	15–22 %	>10 %

Table 2
Sensitivity of gases at different wavelength *w.r.t* AGST.

Gases	Wavelength Region (650–1000 nm)	Wavelength Region (1000–2500 nm)
Liquid Ammonia	15–41 %	<3 %
Liquid methane	12–32 %	<5 %
Carbon Dioxide	11–24 %	<6 %
Carbon Monoxide	19–32 %	>10 %

At lower wavelengths, neither Si nor SiO_2 exhibit this characteristic. There is a considerable fluctuation in the amount of light reflected by Si and SiO_2 at lower wavelengths with less reflectivity. Fig. 2(b) shows that there is negligible change in the power absorption, tending almost to zero if Si and SiO_2 are used as substrates in the NIR and SWIR regions. From this figure, one can easily see that the PCMs (*i.e.,* CGST and AGST) have significant variations in the power absorption curve. The absorbed power increases by 50% from the crystalline to the amorphous phase at a lower wavelength, then in the mid-wavelength range, there is nearly equal absorption, and finally, at a higher wavelength, there is a notable increase in absorbed power from the amorphous to the crystalline phase. Since the PCMs show sensing properties better than CMOS-based sensing (Si and SiO_2), we have further analyzed the sensor from a dimensional point of view by varying the thickness of the PCMs and the radius of the holes in the nanoporous structure.

From Fig. 3, it is observed that the circular-shaped nanoholes have better reflectivity as compared to the square-shaped nanoholes. Since the overall area of the nano-hole square is greater than the nanohole circle (*i.e.,* more exposed area), the overall reflection is less in the case of the nanohole square. So, we have focused on the nanohole circle for further discussion.

As illustrated in Fig. 4(a), as the radius of the circle increases, the reflectivity in crystalline and amorphous phases shifts to lower values due to the lowering of the overall refractive index of the nanoporous structure. Lower wavelengths cause the reflectivity to drop by 3% in the crystalline phase and 19% in the amorphous phase when the radius increases from 0.1 μm to 0.15 μm. As we move from the crystalline to the amorphous phase, a 3% drop in reflection is observed. In the SWIR region, the drop in reflectivity is very low with increasing radius as compared to the NIR region. Fig. 4(b) illustrates the increase in power absorption due to the use of PCMs with the increase in the radius of the circle. When the exposed area increases, power absorption increases significantly in both the crystalline and amorphous phases at shorter wavelengths, with minimal alterations occurring in the mid- and higher-wavelength regions. The amorphous phase shows an increase of 75% in power absorption, which is very high as compared with a 15% increase in the case of the crystalline phase. On the phase change from amorphous to crystalline, we can observe a difference of about 40%.

The thickness change in PCM brings the oscillatory nature of the optical response. For less thickness, the oscillation is negligible. Fig. 5(a) clearly shows how the fluctuations in the reflectivity curve have been observed. As the thickness of the GST (both CGST and AGST) increases, we can observe fluctuations in the reflectivity curve, as seen in Figs. 5(a) and 5(b).

The increase in reflectivity at certain wavelengths is due to the strong confinement of the electric field at the interface due to SPR. This tends to increase the overall reflection. When the frequency of the evanescent wave and the device coincide, resonance causes a decline in reflection and an increase in power absorption at that wavelength. The steepest increase is found at the lowest thickness, and a decreasing slope is detrimental to sustained detection. When compared to the amorphous phase, the crystalline phase oscillates less. Figs. 6(a) and 6(b) indicate that the wavelength area between 1.5 μm and 2.0 μm exhibits quick decrease in reflection and rise in power absorption. The fluctuations become more prominent as we move into the SWIR region.

The selectivity of the gases with respect to the air is quite low, as seen from Figs. 7(a) and 7(b) for the Au-AGST-SiO_2 interface. The selectivity is below 4% for wavelengths above 1000 nm for all gases except carbon monoxide. All of the gases, however, exhibit greater selectivity in the lower wavelength range of 650 nm to 850 nm than in the higher wavelength range. Carbon monoxide constantly shows better selectivity in the complete wavelength spectra, which is above 10%. At lower wavelengths, liquid ammonia has the best selectivity among all the gases, which is above 15%. The gases show sustainable behavior at higher wavelengths. Since there are noticeable variations in the lower wavelength range between 650 nm and 1000 nm, it is simple to identify each gas. Liquid ammonia has the highest sensitivity among all the gases, which is close to 40% at 650 nm. Over 10% sensitivity is seen across the whole wavelength spectrum in carbon monoxide.

The selectivity and sensitivity of various gases *w.r.t* AGST in complete wavelength spectra are listed in Tables 1 and 2 respectively.

The selectivity of all gases, namely carbon dioxide, carbon monoxide, liquid methane, and liquid ammonia, is fairly low in comparison to air due to the low difference in the overall reflection curve, as shown in Fig. 8(b) for the Au-CGST-SiO_2 interface. The selectivity of all the gases with respect to air is less than 10% in the 750 nm to 2500 nm wavelength region. Hence, sustainable behavior is observed at a higher wavelength. There are significant changes in the lower wavelength region from 650 nm to 750 nm; hence, it is easy to distinguish all the gases from each other. Liquid ammonia shows the highest selectivity among all the gases in the
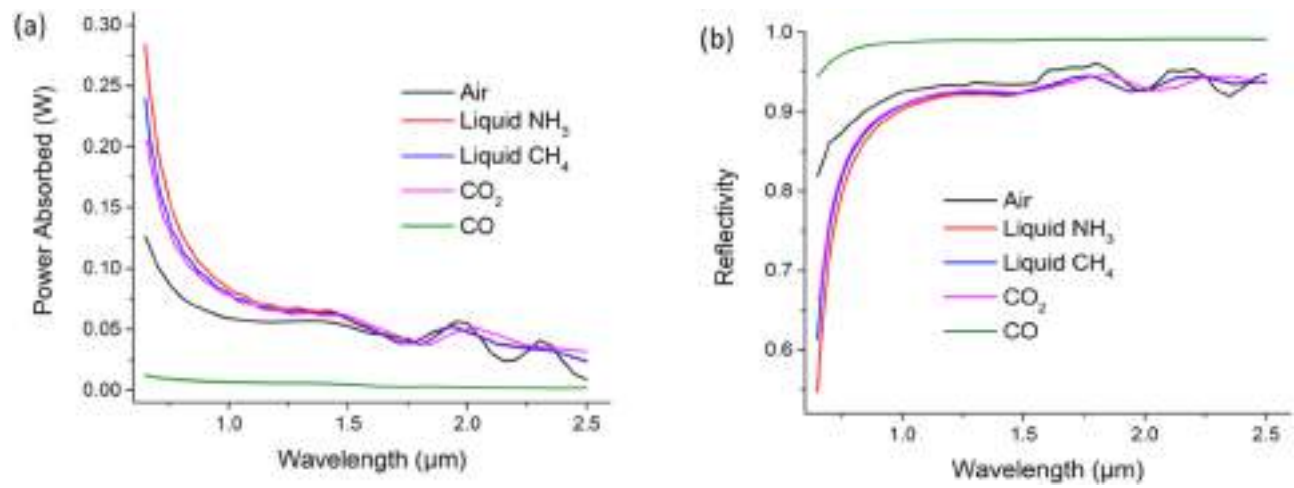
Fig. 8. Variations in (a) Power Absorption (b) Reflectivity of Au-CGST-SiO$_2$ for different gases at 100 nm thickness when the radius of the circle is 0.150 μm.

Table 3

Selectivity of gases at different wavelength *w.r.t.* CGST.

Gases	Wavelength Region (650 nm to 750 nm)	Wavelength Region (750 nm to 2500 nm)
Liquid Ammonia	10–25 %	<8 %
Liquid Methane	9–19 %	<6 %
Carbon Dioxide	7–14 %	<7 %
Carbon Monoxide	9–13 %	<8 %

Table 4

Sensitivity of gases at different wavelength *w.r.t* CGST.

Gases	Wavelength Region (650 nm to 750 nm)	Wavelength Region (750 nm to 2500 nm)
Liquid Ammonia	12–32 %	<4 %
Liquid Methane	9–23 %	<3 %
Carbon Dioxide	8–17 %	<3 %
Carbon Monoxide	10–17 %	<7 %

wavelength region from 650 nm to 750 nm, which varies from 10% to 25%. All other gases, apart from liquid ammonia, show relatively low selectivity. Liquid ammonia has the highest sensitivity among all the gases in the lower wavelength regions of 650 nm to 750 nm.

The selectivity and sensitivity of various gases in complete wavelength spectra *w.r.t.* CGST are listed in Tables 3 and 4, respectively.

There is a rise in reflection from 40% to 90% in the region of 650 nm to 1000 nm. A rise in reflection from 50% to 90% and 20–80% can also be shown in Fig. 9(a) when the material layer (PCM-Metal and Metal-PCM) for CGST and AGST, respectively, is switched. Therefore, CGST is a better sensing material than AGST. While Metal-PCM exhibits a flat spectral response, making it sustainable, PCM-Metal exhibits a wide range of wavelength fluctuations, making it unsustainable. The maximum reflection peak also shifts from 1200 nm to 1700 nm during the phase change from amorphous to crystalline. AGST displays the greatest absorption peak at 1500 nm, while CGST displays the minimum absorption peak at 1800 nm.

We can observe the peak reflection at a wavelength of 1700 nm for liquid ammonia, air, and liquid methane, whereas for carbon dioxide and carbon monoxide, the peak reflection shifts to 1800 nm and 1500 nm, respectively. The device's sensitivity has been greatly increased by switching up the materials and etching holes on the GST surface as opposed to the metal surface, mostly because of the impact of SPR. Carbon monoxide shows a maximum sensitivity of about 58% in the wavelength region from 2000 nm to 2500 nm. Moreover, carbon monoxide has the highest selectivity in the wavelength above 2000 nm, at roughly 58%. Fig. 10 & 11

Compared to carbon dioxide and carbon monoxide, liquid ammonia and liquid methane have comparatively low selectivity and sensitivity. The maximum peak is due to surface plasmon resonance, which enhances the overall reflectivity of the sensing element. All of the gases have significant selectivity at lower wavelengths, making it simple to distinguish one gas from the mixture of gases. The selectivity and sensitivity of various gases in complete wavelength spectra *w.r.t.* CGST-Metal are listed in Tables 5 and 6, respectively.

The sensitivity of the interchanged structure (GST-Metal) is better as compared to Metal-GST. This structure exhibits sensitivity both in the higher wavelength areas and at lower wavelengths. With the exception of carbon monoxide, which has an absorption peak at 1300 nm wavelength, all gases have a maximum absorption peak at 1500 nm wavelength. Comparing their sensitivity and selectivity to other gases, they are fairly high. Carbon monoxide shows a maximum sensitivity of 91% at the 1600 nm wavelength. The selectivity of carbon monoxide is also very good, being greater than 10% in the complete wavelength spectra. Before carbon monoxide, detection of carbon dioxide is also possible at a discrete wavelength, *i.e.,* a sensitivity of 40% at the 1600 nm wavelength.

However, liquid ammonia and liquid methane show poor selectivity. In lower-wavelength regions, the sensitivity of all the gases is high. Liquid ammonia and liquid methane have very low selectivity and sensitivity (less than 4% at higher wavelengths). The selectivity and sensitivity of various gases in complete wavelength spectra *w.r.t.* AGST-Metal are listed in Tables 7 and 8, respectively.

Table 9 displays the results of a compatibility analysis performed on the proposed work and other related works.

4. Conclusions

The nanoporous material consisting of the different substrates (Si, SiO$_2$, Ge$_2$Sb$_2$Te$_5$) has been analyzed using the *Lumerical* FDTD tool. The optical properties of the structure (*i.e.,* reflectivity, power absorption, and electric field variations) are carefully observed by using different geometric arrangements of holes in the metal layer as well as a dielectric layer. The periodicity of the structure is fixed at nine holes per material. We have also analyzed the structure by changing the thickness of the phase change material (*i.e.,* Ge$_2$Sb$_2$Te$_5$). The variation of optical properties on exposure to different gaseous mediums is plotted. Calculations are made about the sensitivity and selectivity of these gases towards air in the wavelength range of 650 nm to 2500 nm. Of all the gases, liquid ammonia has the best selectivity (almost 29 %) between 650 and 1000 nm, while carbon monoxide has the highest sensitivity (32 %). Phase change materials show better optical response as compared to Si and SiO$_2$. The Ge$_2$Sb$_2$Te$_5$ sensor outperforms the MOS-based sensor due to its flat spectrum response and superior sensing capabilities. If holes are made in the substrate instead of the metal layer, the sensitivity of the sensor is enhanced due to surface plasmon resonance. The interchanging of layers increased the sensitivity of all the gases. With a sensitivity of 78% and a selectivity of 40 %, carbon monoxide exhibits the highest values. The dielectric-metal structure is
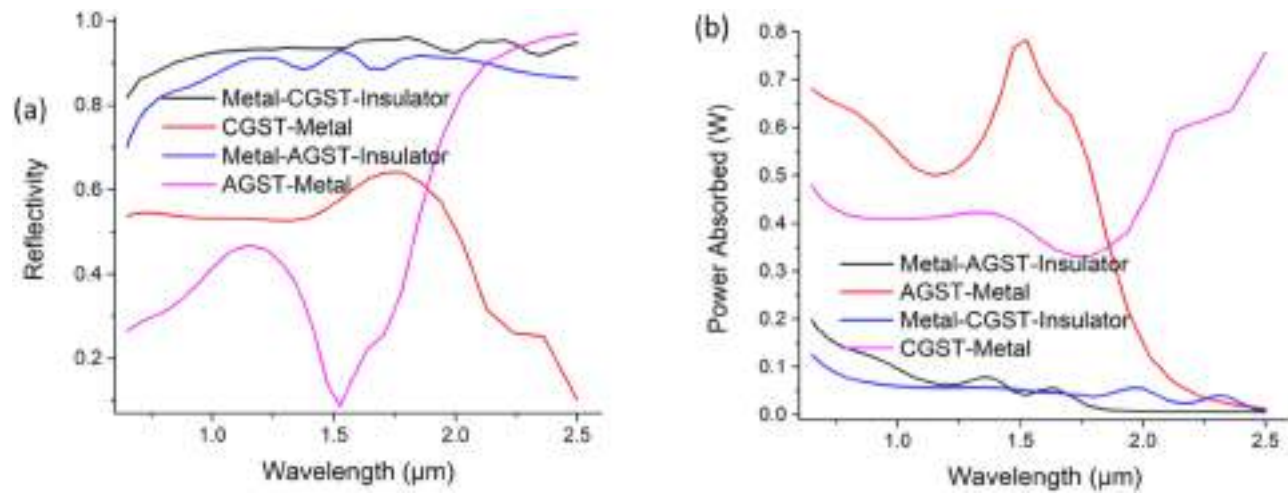
Fig. 9. Variations in (a) Reflectivity and (b) Power Absorption of Au-CGST-SiO$_2$, Au- AGST-SiO$_2$, CGST-Au, AGST-Au at 100 nm thickness when the radius of the circle is 0.150 μm.

Fig. 10. Variations in (a) Reflectivity and (b) Power Absorption of CGST-Au for different gases at 100 nm thickness when the radius of the circle is 0.150 μm.

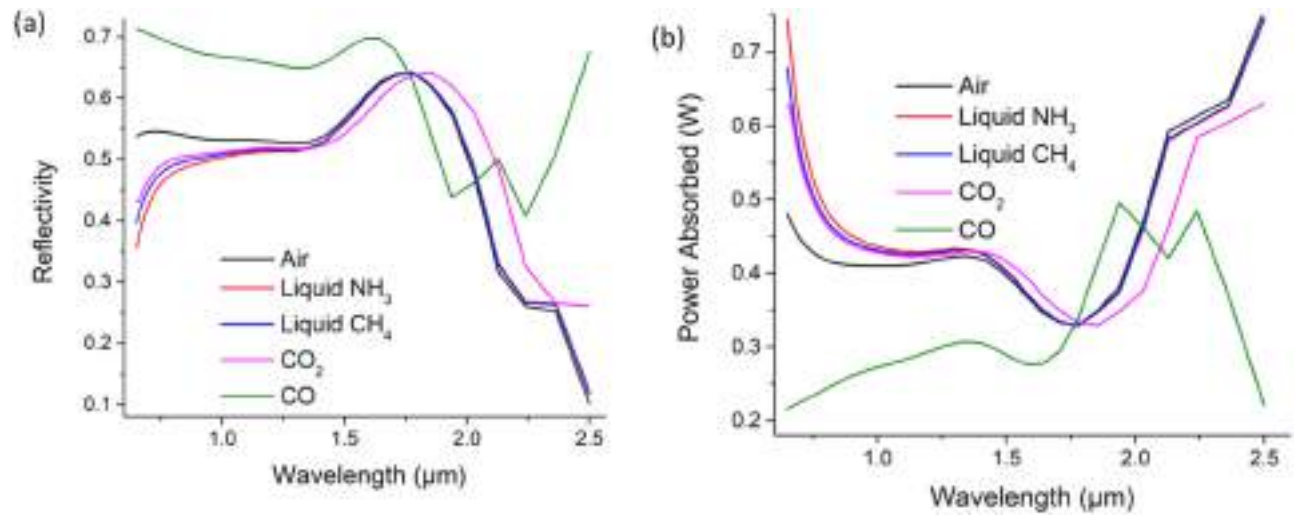**Fig. 11.** Variations in (a) Reflectivity and (b) Power Absorption of AGST-Au for different gases at 100 nm thickness when the radius of the circle is 0.150 μm.
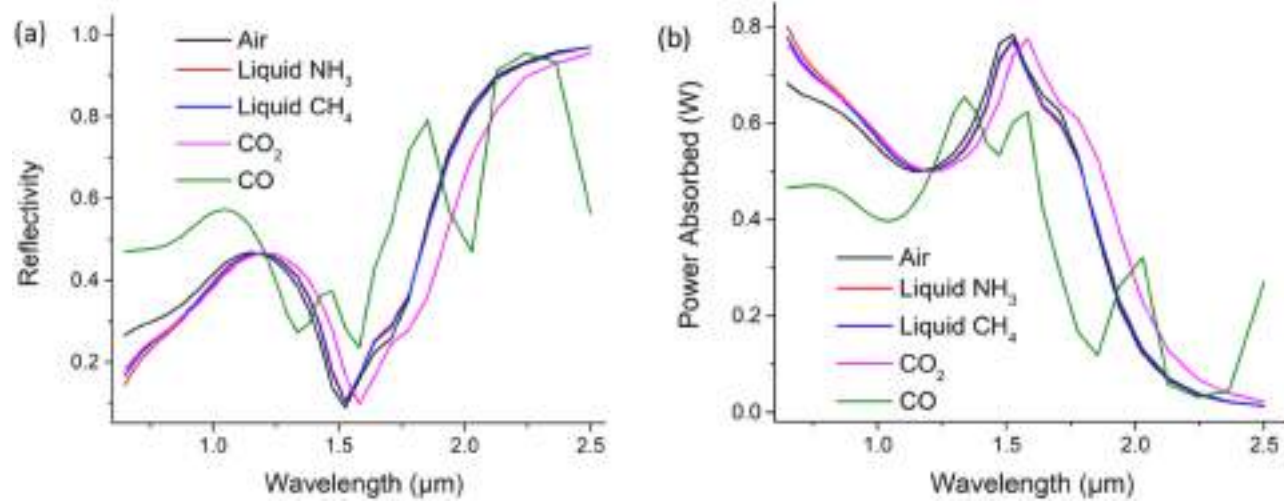
Table 5

Selectivity of gases at different wavelength *w.r.t.* CGST-Metal.

Gases	Wavelength Region(650 nm to 800 nm)	Wavelength Region(800 nm to 2000 nm)	Wavelength Region(2000 nm to 2500 nm)
Liquid Ammonia	9–18 %	<6 %	<1 %
Liquid Methane	10–14 %	<4 %	<1 %
Carbon Dioxide	9–11 %	<3 %	14–16 %
Carbon Monoxide	16–19 %	>15 %	57 %-60 %

Table 6

Sensitivity of gases at different wavelength *w.r.t* CGST-Metal.

Gases	Wavelength Region(650 nm to 800 nm)	Wavelength Region(800 nm to 2000 nm)	Wavelength Region(2000 nm to 2500 nm)
Liquid Ammonia	18–33 %	<2 %	18 %
Liquid Methane	15–26 %	<3 %	15 %
Carbon Dioxide	9–19 %	<4 %	53 %
Carbon Monoxide	27–32 %	>20 %	58 %

Table 7

Selectivity of gases at different wavelength *w.r.t.* AGST-Metal.

Gases	Wavelength Region(650 nm to 800 nm)	Wavelength Region(800 nm to 2000 nm)	Wavelength Region (2000 nm to 2500 nm)
Liquid Ammonia	7–12 %	<4 %	<1 %
Liquid Methane	7–9 %	<3 %	<1 %
Carbon Dioxide	5–7 %	<4 %	<10 %
Carbon Monoxide	17–20 %	>10 %	Up to 40 %

Table 8

Sensitivity of gases at different wavelength *w.r.t.* AGST-Metal.

Gases	Wavelength Region(650 nm to 800 nm)	Wavelength Region(800 nm to 2000 nm)	Wavelength Region (2000 nm to 2500 nm)
Liquid Ammonia	24–45 %	<2 %	<12 %
Liquid Methane	21–37 %	<1 %	<10 %
Carbon Dioxide	19–29 %	Up to 40 %	<10 %
Carbon Monoxide	57–77 %	>15 %	Up to 46 %

Table 9

Comparison of different similar works on gas-sensing application.

Sr.No.	Structure	Material	Gases	Sensitivity/Selectivity	Ref.
1	'+'	Metamaterial Perfect Absorber on Si	CO_2	41%	[46]
2	Nanorods	Polyhexamethylene biguanide polymer deposited on silicon	CO_2	17.3%	[47]
3	Nano-discs	Au(nano-disc)/SiO_2(spacer)/$LiTO_3$/ Au	CO, CO_2, CH_4	104 PPM/38%/44%	[48]
4	Nano-Holes	Au/Cr/BK_7	$NH3/N_2$	1541PPM	[49]
5	Nanoparticles	AL/SiO2/ZnO/Au-NP	CO_2	874 nm/RIU	[50]
6	Nano-Holes	SiO_2/GST/Au	CO, CO_2, NH_3, CH_4	78%/40%	This work

better than the metal-dielectric structure for sensing gases.

CRediT authorship contribution statement

Shirish Tripathi: Writing – original draft, Visualization, Formal analysis, Data curation, Conceptualization. **Ritesh Kumar Mishra:** Writing – review & editing, Validation, Supervision, Conceptualization.

Declaration of Competing Interest

The authors declare that they have no known competing financial interests or personal relationships that could have appeared to influence the work reported in this paper.

Data Availability

Data will be made available on request.

References

[1] G.F. Fine, L.M. Cavanagh, A. Afonja, R. Binions, Metal oxide semi-conductor gas sensors in environmental monitoring, Sensors 10 (2010) 5469–5502, https://doi.org/10.3390/s100605469.

[2] X. Liu, S. Cheng, H. Liu, S. Hu, D. Zhang, H. Ning, A survey on gas sensing technology, Sensors 12 (2012) 9635–9665, https://doi.org/10.3390/s120709635.

[3] J. Zhang, X. Liu, G. Neri, N. Pinna, Nanostructured materials for room-temperature gas sensors, Adv. Mater. 28 (2016) 795–831, https://doi.org/10.1002/adma.201503825.

[4] S. Tripathi, V.Srivastava Sunny, R.K. Mishra, Tuning of resonant mode properties of photonic crystal nanocavities using $Ge_2Sb_2Te_5$ phase-change material, Indian J. Phys. 97 (2023) 3637–3642, https://doi.org/10.1007/s12648-023-02661-8.

[5] V. Srivastava, P. Mishra, Sunny, Investigations on transient regime of $Ge_2Sb_2Te_5$-based vertical photodetector integrated with silicon-on-insulator waveguide, Photonics Nanostruct. 40 (2020) 100796, https://doi.org/10.1016/j.photonics.2020.100796.

[6] M. Rudé, V. Mkhitaryan, A.E. Cetin, T.A. Miller, A. Carrilero, S. Wall, F.J.G. de Abajo, H. Altug, V. Pruneri, Ultrafast and broadband tuning of resonant optical nanostructures using phase-change materials, Adv. Opt. Mater. 4 (2016) 1060–1066, https://doi.org/10.1002/adom.201600079.

[7] G. Wamg, Q. Shi, F. Chen, Y. Yu, Gas sensor based on multiple Fano resonances in metal-insulator-metal waveguide resonator system, J. Optoelectron. Adv. Mater. 24 (2022) 323–331.

[8] F. Chen, L. Sun, H. Zhang, J. Li, C. Yu, Tunable optical absorption based on plasmonic nanostructure assisted by phase-changing material, Optik 189 (2019) 72–80, https://doi.org/10.1016/j.ijleo.2019.05.082.

[9] J. Homola, Surface plasmon resonance sensors for detection of chemical and biological species, 462–93, Chem. Rev. 108 (2008), https://doi.org/10.1021/cr068107d.

[10] B. Lee, S. Roh, J. Park, Current status of micro- and nano-structured optical fiber sensors, Opt. Fiber Technol. 15 (2009) 209–221, https://doi.org/10.1016/j.yofte.2009.02.006.

[11] A. Nooke, U. Beck, A. Hertwig, A. Krause, H. Krüger, V. Lohse, D. Negendank, J. Steinbach, On the application of gold based SPR sensors for the detection of hazardous gases, Sens Actuators B Chem. 149 (2010) 194–198, https://doi.org/10.1016/j.snb.2010.05.061.

[12] T.T. Goodrich, H.J. Lee, R.M. Corn, Direct detection of genomic DNA by enzymatically amplified SPR imaging measurements of RNA microarrays, J. Am. Chem. Soc. 126 (2004) 4086–4087, https://doi.org/10.1021/ja039823p.

[13] M.A. Cooper, Optical biosensors in drug discovery, Nat. Rev. Drug Discov. 1 (2002) 515–528, https://doi.org/10.1038/nrd838.

[14] Y. Fang, Label-free cell-based assays with optical biosensors in drug discovery, 583–95, Assay. Drug Dev. Technol. 4 (2006), https://doi.org/10.1089/adt.2006.4.583.

[15] V. Koubová, E. Brynda, L. Karasová, J. Škvor, J. Homola, P. Dostálek, P. Tobiška, J. Rošický, Detection of foodborne pathogens using surface plasmon resonance biosensors, Sens Actuators B Chem. 74 (2001) 100–105, https://doi.org/10.1016/S0925-4005(00)00717-6.

[16] J.S. Schildkraut, Long-range surface plasmon electrooptic modulator, Appl. Opt. 27 (1988) 4587, https://doi.org/10.1364/AO.27.004587.

[17] P.J. Kajenski, Tunable optical filter using long-range surface plasmons, Opt. Eng. 36 (1997) 1537, https://doi.org/10.1117/1.601376.

[18] Y.-D. Su, S.-J. Chen, T.-L. Yeh, Common-path phase-shift interferometry surface plasmon resonance imaging system, Opt. Lett. 30 (2005) 1488, https://doi.org/10.1364/OL.30.001488.

[19] R.W. Wood, On a Remarkable case of uneven distribution of light in a diffraction grating spectrum, Proc. Phys. Soc. Lond. 18 (1902) 269–275, https://doi.org/10.1088/1478-7814/18/1/325.

[20] D. Bohm, D. Pines, A Collective description of electron interactions. I. Magnetic interactions, Phys. Rev. 82 (1951) 625–634, https://doi.org/10.1103/PhysRev.82.625.

[21] R.H. Ritchie, Plasma losses by fast electrons in thin films, Phys. Rev. 106 (1957) 874–881, https://doi.org/10.1103/PhysRev.106.874.

[22] A. Otto, Excitation of nonradiative surface plasma waves in silver by the method of frustrated total reflection, Z. Phys. A Hadrons Nucl. 216 (1968) 398–410, https://doi.org/10.1007/BF01391532.

[23] E. Kretschmann, H. Raether, Notizen: radiative decay of non radiative surface plasmons excited by light, Z. F. üR. Naturforsch. A 23 (1968) 2135–2136, https://doi.org/10.1515/zna-1968-1247.

[24] B. Liedberg, C. Nylander, I. Lunström, Surface plasmon resonance for gas detection and biosensing, Sens. Actuators 4 (1983) 299–304, https://doi.org/10.1016/0250-6874(83)85036-7.

[25] B.D. Gupta, R.K. Verma, Surface plasmon resonance-based fiber optic sensors: principle, probe designs, and some applications, J. Sens 2009 (2009) 1–12, https://doi.org/10.1155/2009/979761.

[26] R.C. Jorgenson, S.S. Yee, A fiber-optic chemical sensor based on surface plasmon resonance, Sens Actuators B Chem. 12 (1993) 213–220, https://doi.org/10.1016/0925-4005(93)80021-3.

[27] Y. Zhao, R. Tong, F. Xia, Y. Peng, Current status of optical fiber biosensor based on surface plasmon resonance, Biosens. Bioelectron. 142 (2019) 111505, https://doi.org/10.1016/j.bios.2019.111505.

[28] A. Hassani, M. Skorobogatiy, Design criteria for microstructured-optical-fiber-based surface-plasmon-resonance sensors, J. Opt. Soc. Am. B 24 (2007) 1423, https://doi.org/10.1364/JOSAB.24.001423.

[29] Y. Zhang, L. Xia, C. Zhou, X. Yu, H. Liu, D. Liu, Y. Zhang, Microstructured fiber based plasmonic index sensor with optimized accuracy and calibration relation in large dynamic range, Opt. Commun. 284 (2011) 4161–4166, https://doi.org/10.1016/j.optcom.2011.04.053.

[30] J.N. Dash, R. Jha, Highly sensitive D shaped PCF sensor based on SPR for near IR, Opt. Quantum Electron 48 (2016) 137, https://doi.org/10.1007/s11082-016-0423-3.

[31] A.K. Mishra, S.K. Mishra, B.D. Gupta, SPR based fiber optic sensor for refractive index sensing with enhanced detection accuracy and figure of merit in visible region, Opt. Commun. 344 (2015) 86–91, https://doi.org/10.1016/j.optcom.2015.01.043.

[32] R. Otupiri, E.K. Akowuah, S. Haxha, Multi-channel SPR biosensor based on PCF for multi-analyte sensing applications, Opt. Express 23 (2015) 15716, https://doi.org/10.1364/OE.23.015716.

[33] B. Gauvreau, A. Hassani, M. Fassi Fehri, A. Kabashin, M.A. Skoro, Sorsbogatiy, photonic bandgap fiber-based surface plasmon resonance sen, Opt. Express 15 (2007) 11413, https://doi.org/10.1364/OE.15.011413, bogatiy, photonic bandgap fiber-based surface plasmon resonance sen.

[34] A. Rifat, G. Mahdiraji, D. Chow, Y. Shee, R. Ahmed, F. Adikan, Photonic crystal fiber-based surface plasmon resonance sensor with selective analyte channels and graphene-silver deposited core, Sensors 15 (2015) 11499–11510, https://doi.org/10.3390/s150511499.

[35] W. Li, F. Xu, S. Cheng, W. Yang, B. Liu, M. Liu, Z. Yi, B. Tang, J. Chen, T. Sun, Six-band rotationally symmetric tunable absorption film based on AlCuFe quasicrystals, Opt. Laser Technol. 169 (2024) 110186, https://doi.org/10.1016/j.optlastec.2023.110186.

[36] W. Li, M. Liu, S. Cheng, H. Zhang, W. Yang, Z. Yi, Q. Zeng, B. Tang, S. Ahmad, T. Sun, Polarization independent tunable bandwidth absorber based on single-layer graphene, Diam. Relat. Mater. 142 (2024) 110793, https://doi.org/10.1016/j.diamond.2024.110793.

[37] Q. Shangguan, Y. Zhao, Z. Song, J. Wang, H. Yang, J. Chen, C. Liu, S. Cheng, W. Yang, Z. Yi, High sensitivity active adjustable graphene absorber for refractive index sensing applications, Diam. Relat. Mater. 128 (2022) 109273, https://doi.org/10.1016/j.diamond.2022.109273.

[38] J. Ma, P. Wu, W. Li, S. Liang, Q. Shangguan, S. Cheng, Y. Tian, J. Fu, L. Zhang, A five-peaks graphene absorber with multiple adjustable and high sensitivity in the far infrared band, Diam. Relat. Mater. 136 (2023) 109960, https://doi.org/10.1016/j.diamond.2023.109960.

[39] H.-D. Jeong, S.-Y. Lee, Tunable Plasmonic absorber using a nanoslit array patterned on a $Ge_2Sb_2Te_5$ -inserted fabry–pérot resonator, J. Light. Technol. 36 (2018) 5857–5862, https://doi.org/10.1109/JLT.2018.2878861.

[40] L. Wu, P. Bai, X. Zhou, E.P. Li, Reflection and transmission modes in nanohole-array-based plasmonic sensors, IEEE Photonics J. 4 (2012) 26–33, https://doi.org/10.1109/JPHOT.2011.2177652.

[41] A.R. Hajiaboli, B. Cui, M. Kahrizi, V. Truong, Optical properties of thick metal nanohole arrays fabricated by electron-beam and nanosphere lithography, Phys. Status Solidi (a) 206 (2009) 976–979, https://doi.org/10.1002/pssa.200881294.

[42] Y. Chen, X. Li, X. Luo, S.A. Maier, M. Hong, Tunable near-infrared plasmonic perfect absorber based on phase-change materials, Photonics Res 3 (2015) 54, https://doi.org/10.1364/PRJ.3.000054.

[43] C.W. Robertson, D. Williams, Optical constants of liquid ammonia in the infrared, J. Opt. Soc. Am. 63 (1973) 188, https://doi.org/10.1364/JOSA.63.000188.

[44] J.V. Martonchik, G.S. Orton, Optical constants of liquid and solid methane, Appl. Opt. 33 (1994) 8306, https://doi.org/10.1364/AO.33.008306.

[45] G.A. Baratta, M.E. Palumbo, Infrared optical constants of CO and CO_2 thin icy films, J. Opt. Soc. Am. A 15 (1998) 3076, https://doi.org/10.1364/JOSAA.15.003076.

[46] A. Lochbaum, A. Dorodnyy, U. Koch, S.M. Koepfli, S. Volk, Y. Fedoryshyn, V. Wood, J. Leuthold, Compact mid-infrared gas sensing enabled by an all-metamaterial design, Nano Lett. 20 (6) (2020) 4169, https://doi.org/10.1021/acs.nanolett.0c00483.

[47] N.L. Kazanskiy, M.A. Butt, S.N. Khonina, Carbon dioxide gas sensor based on polyhexamethylene biguanide polymer deposited on silicon nano-cylinders metasurface, Sensors 21 (2021) 378, https://doi.org/10.3390/s21020378.

[48] H. Tao, A.C. Strikwerda, M. Liu, J.P. Mondia, E. Ekmekci, K. Fan, D.L. Kaplan, W.J. Padilla, X. Zhang, R.D. Averitt, Performance enhancement of terahertz metamaterials on ultrathin substrates for sensing applications, Appl. Phys. Lett. 97 (2010) 261909, https://doi.org/10.1063/1.3533367.

[49] L. Kalvoda, J. Jakoubkova, M. Burda, P. Kwiecien, I. Richter, J. Kopecek, Fiber Optic Sensor, of Ammonia Gas using plasmonic extraordinary optical transmission, Sensors 23 (2023) 4065, https://doi.org/10.3390/s23084065.

[50] A. Elrashidi, E. Traversa, B. Elzein, Highly sensitive ultra-thin optical CO_2 gas sensors using nanowall honeycomb structure and plasmonic nanoparticles, Front. Energy Res. 10 (2022) 909950, https://doi.org/10.3389/fenrg.2022.909950.